Arabian Journal of Chemistry (2022) **15**, 103795

King Saud University

Arabian Journal of Chemistry

www.ksu.edu.sa
www.sciencedirect.com

ORIGINAL ARTICLE

Silver-Cobalt bimetallic nanoparticles to the generation of hydrogen from formic acid decomposition

Elham Shafik Aazam, Zoya Zaheer *

Department of Chemistry, Faculty of Science, P. O. Box 80203, King Abdulaziz University, Jeddah 21589, Saudi Arabia

Received 19 December 2021; accepted 13 February 2022
Available online 16 February 2022

KEYWORDS

Hydrogen generation;
Bimetallic;
Ag-Co;
Formic acid

Abstract The fabrication of cost effective heterogeneous catalysts for the release of hydrogen from hydrogen storage materials is the key technological challenge to the fuel-cell based hydrogen economy. Ag-Co bimetallic NPs were fabricated by using sodium dodecyl sulphate (SDS) and sodium borohydride as stabilizing and reducing agents, respectively. Catalytic activity of SDS-Ag-Co was higher than that of SDS free Ag-Co and monometallic (Ag and Co) due to the electron interactions and synergistic effect between the Ag and Co. Ag_{10}-Co_{90} exhibited the superior catalytic activity, with rate constant of 5.2×10^{-4} s^{-1} at 303 K, activation energy of 46 kJ/mol, activation enthalpy of 44 kJ/mol, activation entropy of −165 J/K/mol, and turn over frequency of 240 h^{-1}. The hydrogen generation rate increased and decreased with in increasing temperature, molar concentration of formic acid, presence of sodium formate, and pH, respectively. The kinetic rate equation can be stated as: rate = -d[formic acid]/dt = k_{obs}[formic acid]$^{0.99}$[$Ag_{50}Co_{50}$]$^{0.98}$, k_{obs} = 2.48×10^{7} exp (−5637.96/RT).

1. Introduction

Hydrogen has been considered as a fuel for various chemical and petrochemical industrial applications. The storage and release of hydrogen have significant impact on the fuel cell based hydrogen economy (Huber et al., 2006; Navarro et al., 2007). Synthesis of transition metal catalysts for the generation of hydrogen from formic acid (Coffey, 1967; Yang et al., 2019), hydrazine (Al-Thubaiti and Khan, 2020; Singh and Xu, 2009), $NaBH_4$ (Al-Thabaiti et al., 2019; Muir and Yao, 2011), dimethylamine-borane (Sen et al., 2017),

* Corresponding author.
E-mail addresses: zzkhan@kau.edu.sa, zoya.zaheer@gmail.com (Z. Zaheer).
Peer review under responsibility of King Saud University.

Production and hosting by Elsevier

https://doi.org/10.1016/j.arabjc.2022.103795
1878-5352

5aluminum-water reaction (Johnson et al., 2010; Irankhah et al., 2018), alcohols (Yao et al., 2008), and others (Luo et al., 2013; Yang et al., 2011) have been the interest of various researchers from many decades. Out of these formic acid is one of the organic liquid hydrogen carrier, and major product of biomass processing, which contains 4.4 wt% and 53 g/L of hydrogen (Yasaka et al., 2006). The low cost, toxicity, easy transport, high density (1.22 g/cm^3), and excellent stability provides advantages for the practical use of formic acid. Formic acid can be generated as a by-product from bio-refinery systems. Its decomposition can be realized via two competitive reactions such as dehydrogenation (desired path I) and dehydration (undesired path II) (Yang et al., 2015).

$$HCOOH \rightarrow CO_2 + H_2 \quad (path\ I) \tag{1}$$

$$HCOOH \rightarrow CO + H_2O \quad (path\ I) \tag{2}$$

In order to obtain highly hydrogen storage capacity, the path II should be avoided. The dehydrogenation reaction can be initiated on bringing the formic acid solution into contact with a suitable catalyst. The decomposition reaction occurs at different rates depending on the nature of the catalyst used and its method of preparation.

For example, Bimetallic palladium/silver nanowires (PdAg NWs/g-C_xN_4) and silver/palladium nanosheets (AgPd/2D g-C_3N_4) modified with schiff-base-rich g-CxN_4 and mesoporous graphitic carbon nitride, respectively, were fabricated and used as a Mott-Schottky catalyst to enhance the photocatalytic dehydrogenation of formic acid under visible light irradiation (Liu et al., 2021; Wan et al., 2020). These investigators suggested that the catalytic activity of bimetallic NPs depends on the nature of the supporting materials. AgPd nanoparticles stabilized with mesoporous graphitic carbon nitride ($Ag_{0.1}Pd_{0.9}$/N-ompg-C_3N_4) were prepared and used as a catalyst to the generation of hydrogen from decomposition of formic acid (Wan et al., 2022). The strong interactions between the AgPd and N-ompg-C_3N_4 and charge transfer from Pd to Ag were responsible for the remarkable higher catalytic activity.

Yang et al. prepared Pd-based nanoalloy of Ag, Au, Cu, Ir, Pt, Ni and Rh and used as a catalysts for the dehydrogenation of formic acid (Yang et al., 2019). Coffey described the use of Pt-, Ru- and Ir-phosphine complexes on the hydrogen generation from formic acid (Coffey, 1967). Tedsree et al. used AgNPs coated with a thin layer of Pd (core-shell bimetallic NPs) for the dehydrogenation of formic acid (Tedsree et al., 2011). The catalytic activity of a catalyst depends on the number of atoms (Liu et al., 2014; Ben Aziza et al., 2014), stabilizer (Karahan and Ozkar, 2015; Zaheer et al., 2019), supported materials (Zacharska et al., 2016; Zaheer, 2021), and metal-organic frame works (Grad et al., 2019; Yadav and Xu, 2013). Generally, mono-metallic (Cu, Pd, Pt, Ir, Ag, Fe, and Ni) nanocatalysts are inactive to the generation of hydrogen from hydrogen storage materials (Singh and Xu, 2009; Guo et al., 2010). The nanocatalysts have more than one metal (bi- and tri-metallic) exhibited superior catalytic activities due to the synergistic effects of different metals, and surface chemistry of NPs (Hu et al., 2012; Wang et al., 2014).

Silver nanoparticles shows a well-defined surface resonance Plasmon (SPR) band at ca. 400–500 in the visible spectra, and their optical properties AgNPs can be tuned by adding suitable other metal as well as capping agent (Alsubaie et al., 2021; Zaheer and Albukhari, 2020). Silver NPs get an edge over other due to the SPR band as well as different applications in industries, medicine, and water purification, detection of diseases, sensor, catalysis, and generation of hydrogen. Pd-Ag (alloy NPs) (yang et al., 2019) and Ag@Pd (core-shell NPs) (Tedsree, et al., 2011) shows different catalytic activities for the generation of hydrogen from formic acid dehydrogenation. The alloy materials, and core-shell NPs exhibit excellent and poor catalytic activity for hydrogen generation, whereas the physical mixture of the monometallic NPs are catalytically inactive (Singh and Xu, 2013).

Shen et al. prepared metal organic frame work capped Cobalt@-palladium core shell bimetallic NPs for the dehydrogenation of formic acid (Shen et al., 2015). The tri-metallic alloys such as CoAuPd/C (Wang et al., 2013), MIL101-CoAgPd (Cao et al., 2016), and nitrogen doped PdCoNi/C (Dong et al., 2019) were synthesized under different conditions and used as a catalyst for the formic acid decomposition. Based on these findings, it was suggested that the dehydrogenation of formic acid should be catalyzed by the combined effects of all metals present in the nanocatalysts. The literature is replete with the investigations of the use of various noble-metal and non-noble metal NPs as a catalyst to the generation of hydrogen (Yang et al., 2019; Tedsree et al., 2011; Dong et al., 2019), but the kinetics of formic acid decomposition with Ag-Co NPs has been neglected. The dehydrogenation of formic acid with homogeneous catalysts have remained under developed in spite of numerous prominent examples in the literature.

The main objective of this work was to prepare Ag-Co bimetallic NPs with mole ratio (Ag_x-Co_{100-x}) for the enhancement of hydrogen generation from the decomposition of formic acid at room temperature in the absence and presence of sodium formate (SF) as an activator. The metal displacement SDS aided chemical reduction method was employed for the fabrication of $Ag_{50}Co_{50}$ bimetallic NPs by adding an aqueous solution of $NaBH_4$. The presence of SDS on the surface of Ag-Co may make it possible to increase the hydrogen generation due to the strong chelating and binding nature of SDS negative head group. To the best of our knowledge, there is no report on the use of SDS capped Ag-Co bimetallic NPs as a catalyst to the generation of hydrogen from formic acid decomposition.

2. Experimental

2.1. Chemicals

Cobalt nitrate ($Co(NO_3)_2$, 99.9%), sodium borohydride ($NaBH_4$, 99.9%), sodium format (HCOONa, 99.9%), formic acid (HCOOH, 98–100%), hydroxide (NaOH), silver nitrate ($AgNO_3$, 99.9%), and sodium dodecyl sulfate ($C_{12}H_{25}SO_4Na$, ≥99.0%) (all Sigma Aldrich of high quality poducts) were used as received. Milli-Q ultrapure water was used to the preparation of all reagents solution as well as for dilution.

2.2. Synthesis of Ag-Co NPs

In order to prepare AgNPs, the $AgNO_3$ solution (2.0×10^{-3} mol/L) was added in a reaction container containing the SDS solution (8.0 mM). The $NaBH_4$ solution (4.0×10^{-3} mol/L) was added drop-wise to the reaction vessel at room temperature (30 °C) within 5 min. The reaction mixture was then equilibrated in a water bath with constant stirring. The formation of orange color indicates the reduction of Ag^+ ions into the metallic silver (Ag^0) by $NaBH_4$ (Albeladi et al., 2020). In the second step, the Co^{2+} ions (2.0×10^{-3} mol/L) were added into the transparent silver sols in presence of SDS. Co^{2+} ions were reduced on the surface of resulting Ag^0, which leads to the formation of Ag-Co bi-metallic NPs (Khan et al., 2016). The resulting black suspension was collected by centrifugation, washed several times with distilled water and finally dried under vacuum at room temperature for 24 h. The SDS free Ag-Co NPs were also prepared by using the same reaction procedure. The resulted precipitate were washed with deionized water, dried at room temperature, and used as a catalyst to the decomposition of formic acid.

2.3. Characterization of Ag-Co

In order to determine the surface morphology of the Ag-Co, transmission electron microscope (JEM-2200FS, JEOL, and

Japan) was used. For sample preparation, the few drops of Ag-Co suspension were deposited on a carbon-coated copper grid, and dried at room temperature prior to use under TEM operating at 200 kV. The Image J software was used to the evaluation of particle size from the TEM. UV–visible spectroscope provides the preliminary information about the size, shape and size distribution of NPs in an aqueous solution. Therefore, UV–visible spectra of NPs were recorded by measuring the absorbance at 250 to 800 nm on a spectrophotometer (Shimadzu UV–vis multi Spec-1501) with 1 cm quartz cuvettes at different time intervals. X-ray diffractometer (Rigaku X-ray diffractometer (XRD; Rigaku, Japan) was used to determine the crystalline nature of the as prepared Ag-Co with Cu Kα radiation (λ = 1.5406 Å). X-ray photo-electron spectroscopy (XPS, Shimadzu ESCA- 3400) was used to determine the surface metal oxidation states of freshly as prepared SDS-$Ag_{50}Co_{50}$ NPs by using Mg Kα source operating at 10 kV and 10 mA. The silver and cobalt metal contents in the nanocatalyst was determined by inductively coupled plasma-atomic emission spectroscopy (ICP-AES) after the recycle test of the catalyst.

2.4. Generation of hydrogen and carbon dioxide

Hydrogen generation experiment was performed by using a two necked round bottom reaction flask fitted with an outlet tube for collecting evolved hydrogen gas. The formic acid (10 ml of 0.5 M) was added into the reaction vessel containing 0.02 g of Ag_{50}-Co_{50}. The reaction vessel was submerged in a paraffin oil bath held at constant temperature via a temperature probe and heating controller. The progress of the reaction was followed by collecting the hydrogen with water displacement method at different time intervals. In a typical experiment, the outlet was placed under filled graduated cylinder situated in a water-filled tank. The hydrogen gas was measured by recording the water displaced (Al-Thubaiti and Khan, 2020). On the other hand, the generated gases (H_2 + CO_2) was swept out with constant current of pure N_2 gas and passed through a solution of standard $Ba(OH)_2$ to trap the CO_2 gas (CO_2 + $Ba(OH)_2$ → $BaCO_3$ + H_2O). The white precipitate was formed and $Ba(OH)_2$ solution became turbid, indicating the formation of CO_2 along with the H_2 during the formic acid dehydrogenation (Eq.1). The rate constants were calculated by using the Eq. (3) (Al-Thabaiti et al., 2019).

$$k_{obs} = \frac{1}{t}\ln\left(\frac{V_\alpha - V_0}{V_\alpha - V_t}\right) \tag{3}$$

where k = first-order rate constant. V_α, V_0, and V_t are the volume of generated gases (CO_2 and H_2) at different time intervals. The reaction was carried out for 4 h at 40 °C. The turn over frequency (TOF) of the Ag_{50}-Co_{50} was calculated with Eq. (4) at 50% conversion, on the basis of total metal atoms in the catalyst (Chen et al., 2015).

$$TOF = \frac{P_{atom}V(H_2 + CO_2)}{2RTn(Ag + Co)t} \tag{4}$$

where p_{atom} = atmospheric pressure, V_{H2+CO2} = volume of generated CO_2 + H_2, R = universal gas constant (8.314 J/mol/K), T = temperature in Kelvin, n(Ag + Co) = moles of each metal, and t = reaction time in hour.

2.5. Stability and durability of the catalyst

The stability and reusability tests were performed at 30 °C and using an aqueous formic acid solution (0.7 M). After the first experiment, the generation of hydrogen was stopped, the catalyst filtered at room temperature, and it was used in a new kinetic consecutive reaction under the same experimental conditions without further washing. The hydrogen evolution was initiated by adding the same amount of formic acid. This cycle was repeated five times.

3. Results and discussion

3.1. Morphology of Ag-Co

Metal displacement galvanic cell reaction method was used for the synthesis of Ag_{50}-Co_{50} in presence of SDS. In a typical experiment, $AgNO_3$ solution was added in a reaction vessel containing SDS and stirred for 20 min at 30 °C to the complete complex formation between Ag^+ and negative head group of SDS ($-OSO_3^-$). The required amount of freshly prepared $NaBH_4$ solution was added drop-wise with constant stirring. The colorless reaction mixture became orange-yellow, indicating the reduction of Ag^+ ions by $NaBH_4$ (formation of NPs) (Albeladi et al., 2020). UV–visible spectra of AgNPs as a function of time are given in Fig. 1, which shows a sharp well defined SPR band at 420 nm, suggesting the formation of spherical shapes AgNPs. In the next experiment, the Co $(NO_3)_2$ solution was added into the resulting orange colored silver sols and 5.0 ml $NaBH_4$. The yellowish-black suspension was appeared with increasing time (Table 1). The UV–visible spectrum of the resulting silver-cobalt sol was featureless in the whole visible region. The Co^{2+} ions would be reduced on the surface of Ag^0 under potential deposition and Ag-Co NPs were formed. The step-wise synthesis of Ag-Co is given in Scheme 1 (see Scheme 2).

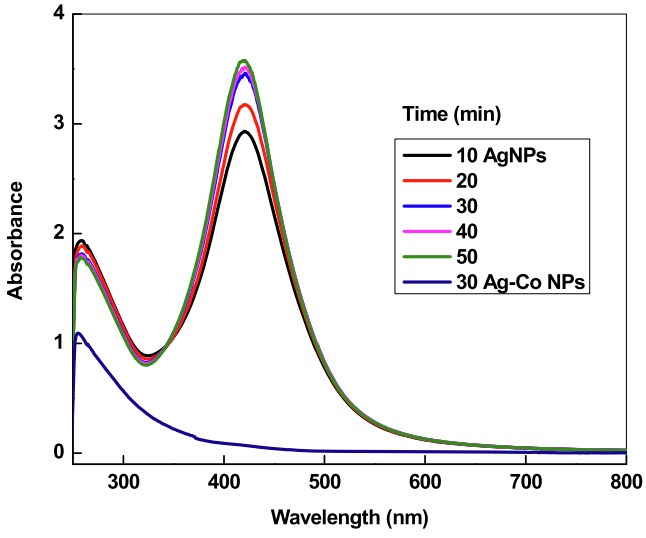

Fig. 1 UV–visible spectra of AgNPs, and $Ag_{50}Co_{50}$ in presence of SDS at 303 K. *Reaction conditions*: molar ratio of Ag^+:Co^{2+} = $Ag_{50}Co_{50}$ = 1:1, [$NaBH_4$] = 0.01 mM, and [SDS] = 8.0 mM.

Table 1 Effect of Ag^{+}, Co^{2+} ions, $NaBH_4$, and SDS on the synthesis of $Ag_{50}Co_{50}$ after 30 min at 303 K.

$[Ag^{+}]$(mM)	$[NaBH_4]$ (mol/L)	SDS (mM)	Observations of Ag-Co
1.0	0.01	0.0	Yellow-white turbidity
	0.01	2.0	Light yellow
	0.01	8.0	Orange (λ_{max} = 425 nm)
$[Co^{2+}]$ in AgNPs			
1.0	0.0	0.0	Orange (λ_{max} = 425 nm)
	0.01	2.0	Gray transparent
	0.01	8.0	Black suspension
	0.01	12.0	Black precipitate

$$Ag^{+} + BH_4^{-} \xrightarrow{SDS} Ag^{0} \quad (5)$$

$$Ag^{0} + Co^{2+} + 2BH_4^{-} + 6H_2O \xrightarrow{SDS} Ag\text{-}Co + 2H_3BO_3 + 7H_2 \quad (6)$$

Scheme 1 Step-wise synthesis of Ag-Co in presence of SDS.

$$CH_3(CH_2)_{11}OSO_3Na \rightleftharpoons CH_3(CH_2)_{11}OSO_3^{-} + Na^{+} \quad (8)$$
(SDS) (DS)

$$[CH_3(CH_2)_{11}OSO_3^{-} + Ag^{+} \rightleftharpoons [CH_3(CH_2)_{11}OSO_3\text{-}Ag] \quad (9)$$
(DS) (DS-Ag ; complex)

$$[CH_3(CH_2)_{11}OSO_3\text{-}Ag] + BH_4^{-} + 3H_2O \longrightarrow CH_3(CH_2)_{11}OSO_3\text{-}Ag^{0} + H_3BO_3 + 3\,H_2 \quad (10)$$
(DS-AgNPs ; λ_{max} = 420 nm)

Scheme 2 Reduction of Ag^{+} into Ag^{0} by $NaBH_4$ with SDS.

Fig. 2A and 2B shows the shows the SEM and TEM images of SDS-Ag-Co NPs, respectively. The Ag-Co are spherical, aggregated to each other, deposited onto the surface, and leads to the formation of layered like surface morphology of metallic Ag_{50}-Co_{50} (Fig. 2A). TEM image indicates the formation of various small size Ag_{50}-Co_{50} (ranging from 10 to 30 nm) with 8.0 mM SDS. The resulting Ag-Co are adsorbed on the surface of each other (Fig. 2B; as indicated by red circle), and large size Ag-Co are formed. Elemental composition was determined by recording SEM-EDX (Fig. 2C and 2D). The resulting NPs consists 50.11 wt% (15.80 at%) and 15.62 wt% (9.02 at%) Ag^{0} and Co^{0}, respectively, along with 3.33 wt% (9.42 at%) C and 30.94 wt% (65.77 at%) O (Fig. 2D), while the amount of Ag^{+} and $Co^{2+}$is 1:1 bulk mole ratio (Gurtu and Bakshi, 2018). The presence of C and O peaks are from the TEM grid and exposure of sample in air during the grid preparation.

X-ray diffraction was carried out with Bragg-Berentano geometry using Cu Kα radiation in the angular range 0 to 90° in the step of 0.02°. The typical XRD patterns for the Ag_{50}-Co_{50} are given in Fig. 3A. The four major peaks at 38.25°, 44.49°, 64.72, and 77.61° are corresponds to the (111), (200), (220), and (311) plans of face centered cubic (*fcc*) silver structure, respectively (JCPDS 04-0783). The crystalline data revealed that the AgNPs was crystalline face centered cubic AgNPs. The XRD patterns of $Ag_{50}Co_{50}$ show the peaks are approximately consistence with the diffraction peaks of Ag (JCPDS 04-0783) (Khan, 2020) and Co (JCPDS 15-0806) (Shen et al., 2015). In addition, a peak was also appeared at 59.5° (220), which might be due to the deposition of Co on the surface of metallic silver. The crystallite size of Ag_{50}-Co_{50} was calculated with Scherrer formula (Eq. (7)).

$$D = \frac{0.9\lambda}{\beta\cos\theta} \quad (7)$$

where, λ = wavelength of x-ray (=1.49 Å), β = full width at half maximum, and θ = Bragg angle.

The crystalline size was found to be 280 Å (28 nm) to the width of (200) diffraction peak at $2\theta = 50.9^{0}$. Fig. 3B show the TGA decomposition of SDS and SDS capped Ag_{50}-Co_{50} under nitrogen atmosphere. The weight loss was observed at ca. 190 °C for SDS and maximum rate of decomposition temperature is at 250 °C. The pure SDS was completely decomposes with the temperature range 200 to 300 °C. For SDS-Ag-Co, strong decomposition endothermic peak was observed at 290 °C. TGA curve shows the persistence of 65% after heating at 700 °C might be due to the metallic Ag and Co.

XPS is used for the analysis of surface oxidation states of Ag and Co in the SDS-$Ag_{50}Co_{50}$. The XPS spectrum of silver in $Ag_{50}Co_{50}$ was shown in Fig. 4A. The silver spectrum can be deconvoluted into two pairs of doublets with binding energies for Ag $3d_{5/2}$ and Ag $3d_{3/2}$ at 367.67 and 373.68 eV, respectively, which could be assigned to states of Ag^{0} (Kosa and Zaheer, 2019). The difference between the two peaks is 6.01 eV, which is consistent with the standard spectra of the element silver (Moulder and Chastain, 1992). For Co 2p XPS spectrum (Fig. 4B), the binding energies for Co $2p_{3/2}$ and Co $2p_{1/2}$ at 778.32 and 793.27 (difference between the two peaks = 14.95 eV) are attributed to the states of Co^{0} (Ortiz-Quinonez and Pal, 2019). These results suggest that Ag-Co composed of metallic Ag^{0} and Co^{0}.

3.2. Role of SDS

SDS is an anionic surfactant and formed various aggregates (monomer, dimer, trimer and micelles) at different concentrations in an aqueous solution. Micelles are formed at the critical micellar concentration of SDS (8.0×10^{-3} mol/L). Therefore, [SDS] = 8.0 mM was used to the preparation of SDS-Ag_{50}-Co_{50} NPs. Surfactant behaves as an electrolyte at lower concentrations, and formed various aggregates. Only 30% of SDS was ionized in an aqueous solution due to the counter ion effect of Na^{+} (Bunton, 2006).

Eq. (8) represents the ionization of SDS. The Ag^{+} formed complex with ionized SDS (Eq. (9) and Ag^{+}. As a result, Ag^{+} was incorporated into the Stern layer of anionic micelles. The coordinated Ag^{+} reacts BH_4^{-} and under goes oxidation-reduction reaction. Finally, orange colored SDS capped AgNPs were formed. In the next step, Co^{2+} ions are deposited on the surface of AgNPs, reduced under potential deposition, and Ag-Co NPs are formed (Scheme 3).

3.3. Catalytic activity results

The catalytic performance of Ag_{50}-Co_{50} on the dehydrogenation of formic acid was studied by monitoring the total evolved

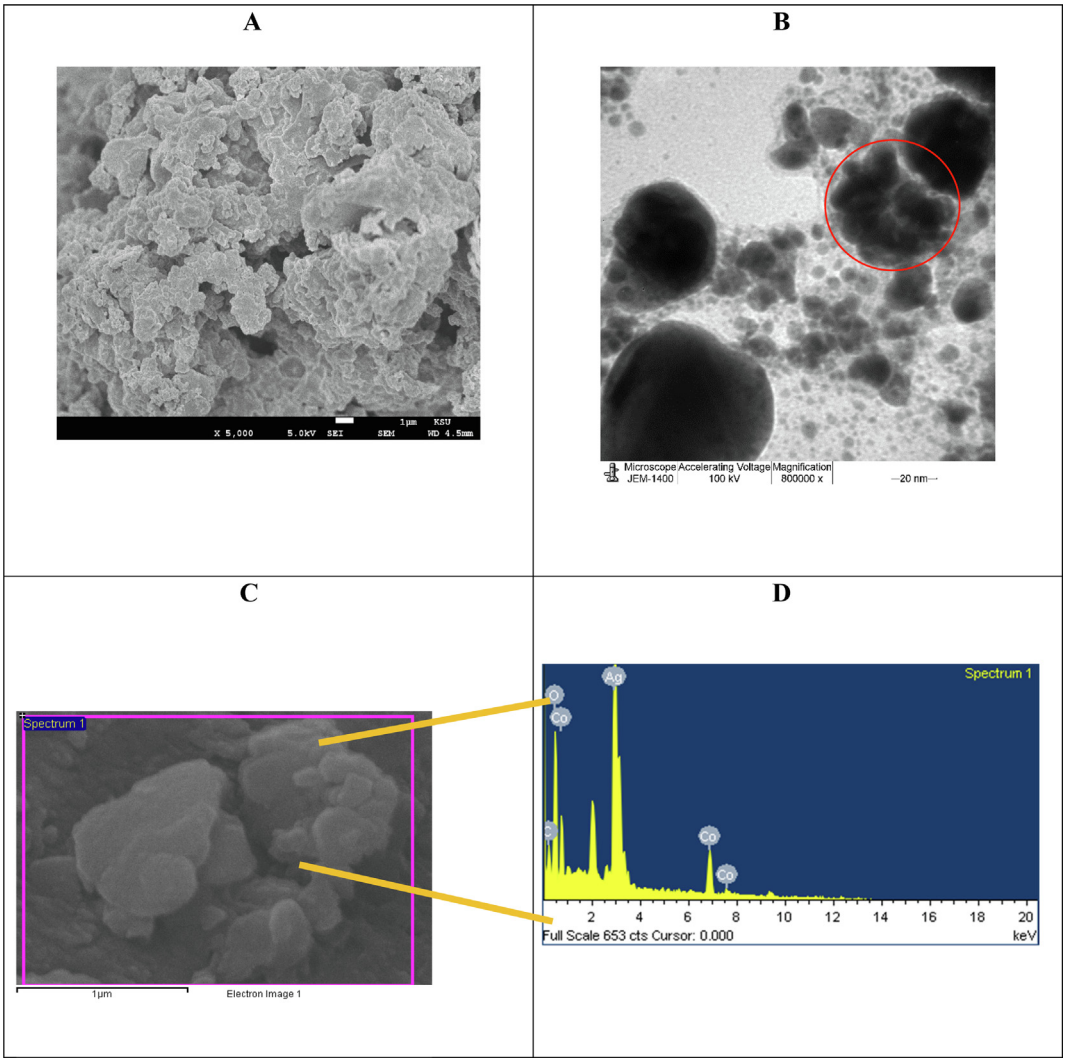

Fig. 2 SEM (A), TEM (B), and SEM-EDX (C and D) of $Ag_{50}Co_{50}$. *Reaction conditions*: molar ratio of Ag^{+}:Co^{2+} = $Ag_{50}Co_{50}$, [$NaBH_4$] = 1.0 mM, and [SDS] = 8.0 mM.

gases under different experimental conditions such as formic acid concentration, amount of catalyst, temperature, pH, and formic acid to sodium formate (SF; promoter) ratio. In the first set of catalytic experiments, the effects of formic acid concentrations (ranging from 0.2 to 1.5 mol/L) on the catalytic activity of Ag_{50}-Co_{50} were evaluated at fixed amount of the catalyst (=0.02 g/L), and temperature (=30 °C). Fig. 5A shows the volume of generated gases increases with increasing the concentration of formic acid. The rate constants were calculated with Eq.(3). The observed results were summarized in Table 2. The plots of $\ln(V_\alpha - V_t)$ versus time indicates that the dehydrogenation of formic acid follow a first-order reaction path(Fig. 5B). Effects of formic acid concentration (ranging from 0.2 to 1.5 mol/L) were also investigated at different temperature (30, 40, 50, and 60 °C) with constant pH = 4.3 (Table 3). The plots of k_{obs} against [formic acid] are linear passing through the origin, indicating the first-order kinetics with formic acid at each temperature (Fig. 5C). The reaction rates were also increases with the amount of the catalyst (Table 2). Khan et al. also reported the first-order kinetics with respect to formic acid concentration for the decomposition reaction at lower concentration (Khan, 2019). In order to see insight into the decomposition of formic acid, the generated gases was passed through the $Ba(OH)_2$ solution to trap the CO_2 and volume of gas was measured at different time intervals. It was observed that the volume of generated gas was reduces to ca. half (Fig. 5D). The CO_2 and H_2 are formed in 1:1 M ratio due to the catalytic dehydrogenation of formic acid (Eq. (1)). In the second set of experiments, the effects of sodium formate were investigated in absence and presence of formic acid. It was observed that the volume of gases increase with increasing the formate concentration at fixed [formic acid] (Table 2). The higher gas generation was observed in the formic acid-format system than that of pure formic acid and formate alone, which might be due to the activation and/or combined effect of formic acid and formate on the catalyst surface (Akbayrak et al., 2017; Jeon and Chung, 2017).

In order to see the effects of SDS concentration on the catalytic activity of SDS-Ag_{50}-Co_{50} NPs toward formic acid decomposition, the nanocatalyst were prepared at

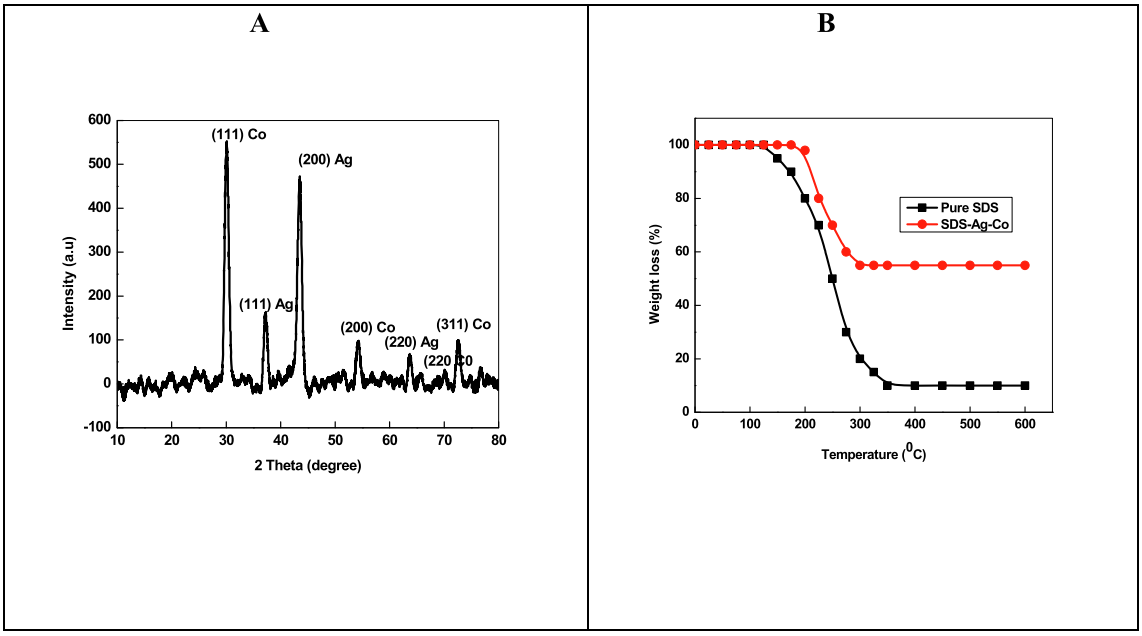

Fig. 3 XRD (A) and TGA (B) of $Ag_{50}Pd_{50}$. *Reaction conditions*: For A- molar ratio of Ag^{+}:Co^{2+} = $Ag_{50}Co_{50}$, [$NaBH_4$] = 1.0 mM, and [SDS] = 8.0 mM.

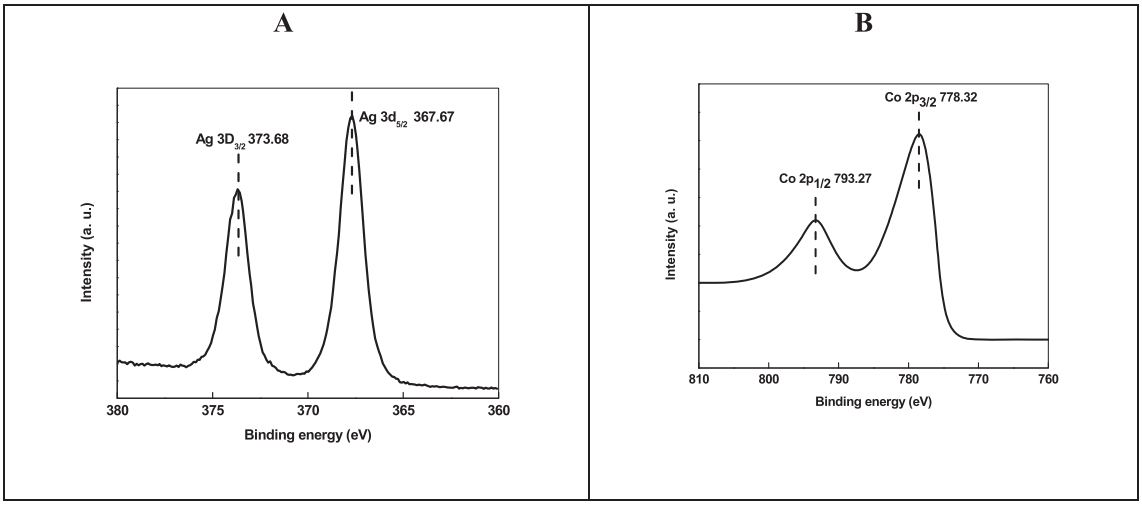

Fig. 4 XPS spectra of Ag 3d (A) and Co 2p (B) for $Ag_{50}Co_{50}$. *Reaction conditions*: For A- molar ratio of Ag^{+}:Co^{2+} = $Ag_{50}Co_{50}$, [$NaBH_4$] = 1.0 mM, and [SDS] = 8.0 mM.

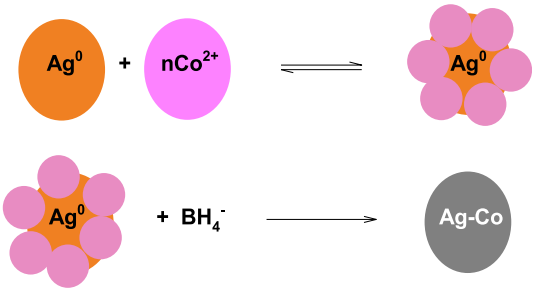

Scheme 3 Formation of Ag-Co NPs after the reduction of Co^{2+} ions onto the Ag^0.

[SDS] = 2.0 mM and 12.0 mM (Table 1). The values of hydrogen generation rate constants were calculated by using various formic acid concentrations. The k_{obs} was found to be ca. 2.2, 3.0, and 5.3 × 10^{-4} s^{-1} for [formic acid] = 0.7, 1.2 and 1.5 mol/L, respectively, at [SDS] = 2.0 mM and 30 °C. Thus, we may state confidently that the stabilizer SDS concentrations have no significant effect on the decomposition of formic acid under our experimental conditions (Table 2).

3.4. Effects of Ag_x-Co_{100-x} and temperature

To investigate the effect of Ag-Co molar ratio on the formic acid dehydrogenation, the different Ag_x-Co_{100-x} catalysts with

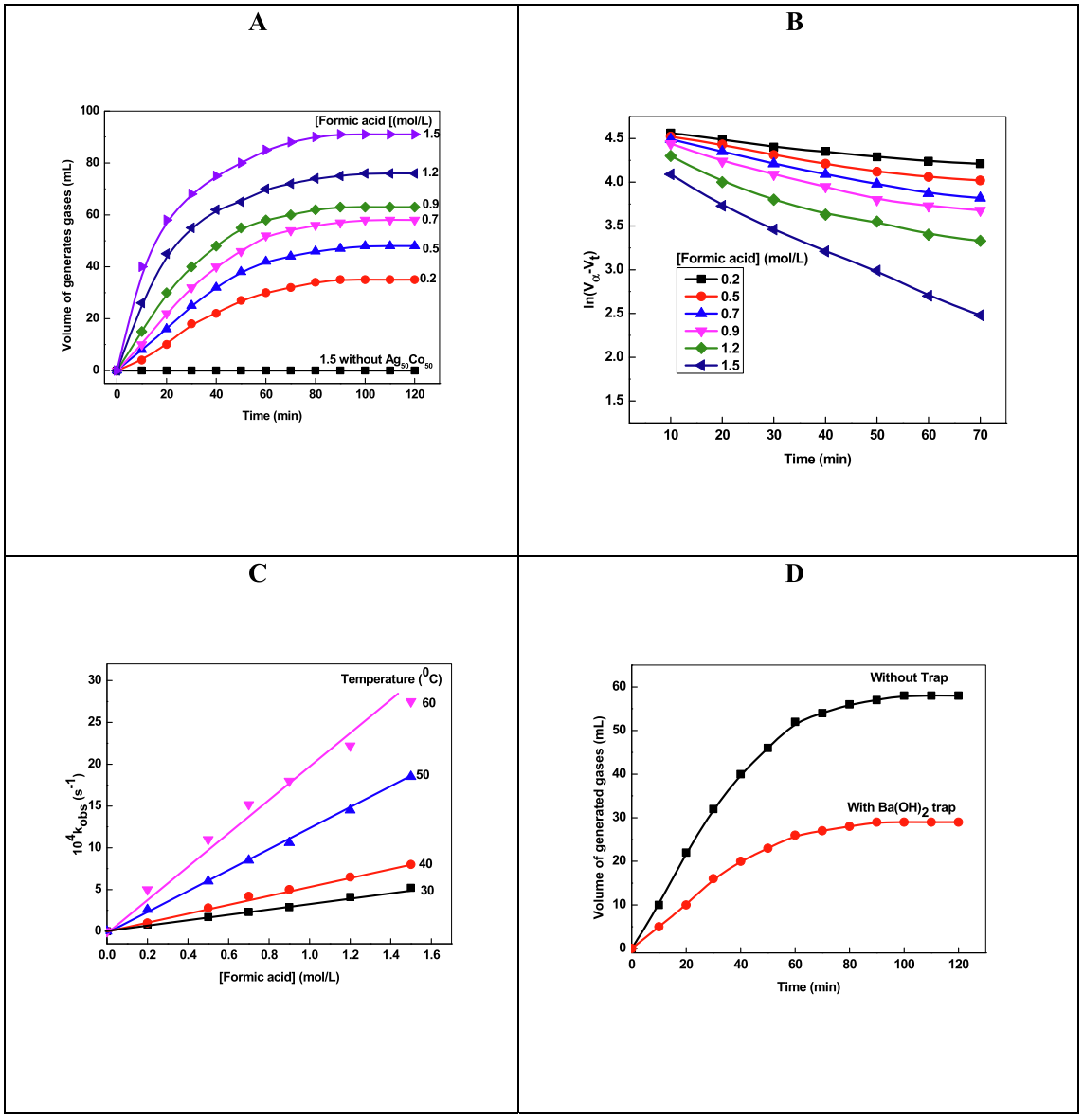

Fig. 5 Reaction-time plots (volume of generated gases versus time (A) and $\ln(V_\alpha\text{-}V_t)$ against time (B)), effects of formic acid on the k_{obs} at different temperatures (C), and results of $Ba(OH)_2$ trap experiment (D) for the dehydrogenation of formic acid by $Ag_{50}Co_{50}$ at 303 K. *Reaction conditions*: $[Ag_{50}Co_{50}]$ = 0.02 g/L, and pH = 4.3.

the range of Ag contents (x = 10 to 90) were prepared and used as a catalyst. The catalytic efficiency increases with increasing the content of Co, which is the key active element in $Ag_x\text{-}Co_{100\text{-}x}$. Fig. 6 shows the effect of different $Ag_x\text{-}Co_{100\text{-}x}$ on the hydrogen generation at various temperatures. In $Ag_x\text{-}Co_{100\text{-}x}$, the formic acid degradation rate was increased and the catalytic performance decreased in the following order: $Ag_{10}Co_{90} > Ag_{20}Co_{80} > Ag_{50}Co_{50} > Ag_{70}Co_{30} > Ag_{90}Co_{10}$. The specific combination of two and/or three metals have significant effect on the reactivity of a catalyst due to the strong synergistic, electronic interactions and structural changes (Shen et al., 2015; Wang et al., 2013; Cao et al., 2016).

It is well known that the activation energy is an important parameter to decide the catalytic activity of the catalyst. Arrhenius and Eyring equations, respectively, were used for the estimation of activation energy (E_a), and enthalpy of activation ($\Delta H^{\#}$), entropy of activation ($\Delta S^{\#}$) (Eqs. (11) and (12)).

$$\ln k_{obs} = \ln A - \frac{E_a}{RT} \tag{11}$$

$$\ln \frac{k_{obs}}{T} = \ln \frac{k_B}{h} + \frac{\Delta S^{\#}}{R} - \frac{\Delta H^{\#}}{RT} \tag{12}$$

where A = Arrhenius factor, R = universal gas constant, T = temperature, k_B = Boltzmann constant, and h = Planck's constant. Arrhenius plots were constructed between the $\ln k_{obs}$ and 1/T, and values of E_a calculated from the slopes of Fig. 6A. The $\Delta H^{\#}$, and $\Delta S^{\#}$ were calculated from the slope and intercept of Eyring plot ($\ln k_{obs}/T$ versus 1/T; Fig. 6B). These results show a good linear approximation from which activation parameters are obtained (Fig. 6; Table 4). The values of E_a are found to be 46, 49, 52, 58 and 66 kJ/mol, respectively, for $Ag_{10}Co_{90}$, $Ag_{20}Co_{80}$, $Ag_{50}Co_{50}$, $Ag_{70}Co_{30}$ and $Ag_{90}Co_{10}$. These results clearly indicates that the molar ratio of both the metals have significant impact on the catalytic effi-

Table 2 Effects of formic acid, sodium formate, pH, and SDS-Ag-Co ($Ag_{50}Co_{50}$) on the dehydrogenation of formic acid ($HCOOH \rightarrow CO_2 + H_2$) at 303 K.

[Formic acid](M)	[SF](M)	[Ag-Co] (g/L)	pH	$10^4 k_{obs}(s^{-1})$
1.5	0.0	0.0	4.3	0.0
1.5	0.02	0.0	4.3	0.0
0.2	0.0	0.02	4.3	1.3
0.5	0.0	0.02	4.3	1.7
0.7	0.0	0.02	4.3	2.3
0.9	0.0	0.02	4.3	2.9
1.2	0.0	0.02	4.3	4.1
1.5	0.0	0.02	4.3	5.2
0.7	0.02	0.02	4.3	2.7
0.7	0.02	0.02	4.3	3.1
0.7	0.02	0.02	4.3	3.5
0.7	0.02	0.02	4.3	3.8
0.7	0.0	0.01	4.3	1.7
0.7	0.0	0.03	4.3	2.9
0.7	0.0	0.04	4.3	5.4
0.7	0.0	0.05	4.3	6.8
0.7	0.0	0.02	6.3	1.9
0.7	0.0	0.02	8.3	1.2
0.7	0.0	0.02	10.3	0.9
0.7	0.0	0.02	12.3	0.7

Table 3 Effects of temperature and values of activation parameters for the dehydrogenation of formic acid ($HCOOH \rightarrow CO_2 + H_2$) at pH 4.3, $[Ag_{50}Co_{50}] = 0.02$ g/L in absence of SF.

[Formic acid] (M)	Temperature (K)				Activation parameters		
	303	313	323	333	E_a (kJ/mol)	$\Delta H^{\#}$ (kJ/mol)	$\Delta S^{\#}$ (kJ/mol)
	10^4 k_{obs} (s^{-1})						
0.2	1.3	1.0	2.6	5.0			
0.5	1.7	2.0	6.0	11.1			
0.7	2.3	4.2	8.5	15.2	52	50	–148
0.9	2.9	5.0	10.6	18.1			
1.2	4.1	6.5	14.5	22.2			
1.5	5.2	8.0	185	27.5			

ciency of Ag-Co. Our calculated activation energy are in accordance to the activation energies of formic acid decomposition in presence of $Pd_{0.6}Co_{0.2}Ni_{0.2}$/N-CN (20.04 kJ/mol) (Dong et al., 2019), Pd/MSC-30 (38 kJ/mol) (Chen et al., 2015), Co-Ag-Pd/RGO (43 kJ/mol) (Chen et al., 2015), Pd/templated carbon (50.8 kJ/mol) (Mihet et al., 2020), Pt/Al_2O_3 (52 kJ/mol) (Ojeda and Iglesia, 2009), Au/Al_2O_3 (51 kJ/mol) (Ojeda and Iglesia, 2009), and Pd-Ag-Fe (66 kJ/mol) (Khan, 2019). Thus we may concluded that the catalytic performance depends on the nature of metal as well as capping and/or supporting materials present on their surfaces.

A SDS free $Ag_{50}Co_{50}$ was prepared with the galvanic cell reaction under similar experimental conditions. The decomposition rate of formic acid was found to be slow (k_{obs} = 1.5, 1.9, and 3.9×10^{-4} s^{-1} for [formic acid] = 0.7, 1.2 and 1.5 mol/L, respectively) than that of SDS capped $Ag_{50}Co_{50}$ (k_{obs} = 2.3, 2.9, and 5.2×10^{-4} s^{-1} for same the [formic acid]) at 30 °C. These observations can be rationalized due to the agglomeration Ag-Co NPs for SDS free nanocatalyst. Surfactant has significant effect on the morphology (shape, size, and the size distribution) of the nanocatalyst and prevents their aggregation. Surfactant capped nanocatalysts provide sufficient catalyst surface for the interaction of formic acid molecules as well as tunes the stability of the reaction intermediates on the catalyst surface (Singh and Xu, 2010; Khan, 2019; Al-Thubaiti and Khan, 2020).

TEM images of SDS-Ag_{10}-Co_{90} and SDS free Ag_{10}-Co_{90} are given in Fig. 7, which indicates that the morphology (shape, size and the size distribution) of Ag-Co depends on the presence of SDS. The Ag-Co NPs are mostly spherical (size ranging from 10 to 60 nm), poly-dispersed, and aggregated to each other in absence of SDS (Fig. 7A). On the other hand, aggregated Ag-Co NPs are formed with 12.0 mM SDS. Inspection of Fig. 7B clearly shows that the various NPs are deposited on to the surface of each other, and bimetallic Ag-Co are formed having heterostructure. TEM images of SDS-AgCo indicates that the size of the NPs depends on the concentration of SDS (Figs. 2 and 7B). The size of Ag-Co decreases with increasing SDS concentration, which might be due to the incorporation of reactants (Ag^+ and Co^{2+}) and NPs into the small volume of anionic micelles.

Bimetallic NPs have complicated structures that can be classified into four types (core-shell, heterostructure, intermetallic or alloyed structure, and multishell structure) based on their mode of mixing (Ferrando, et al., 2008; Liu, et al.,

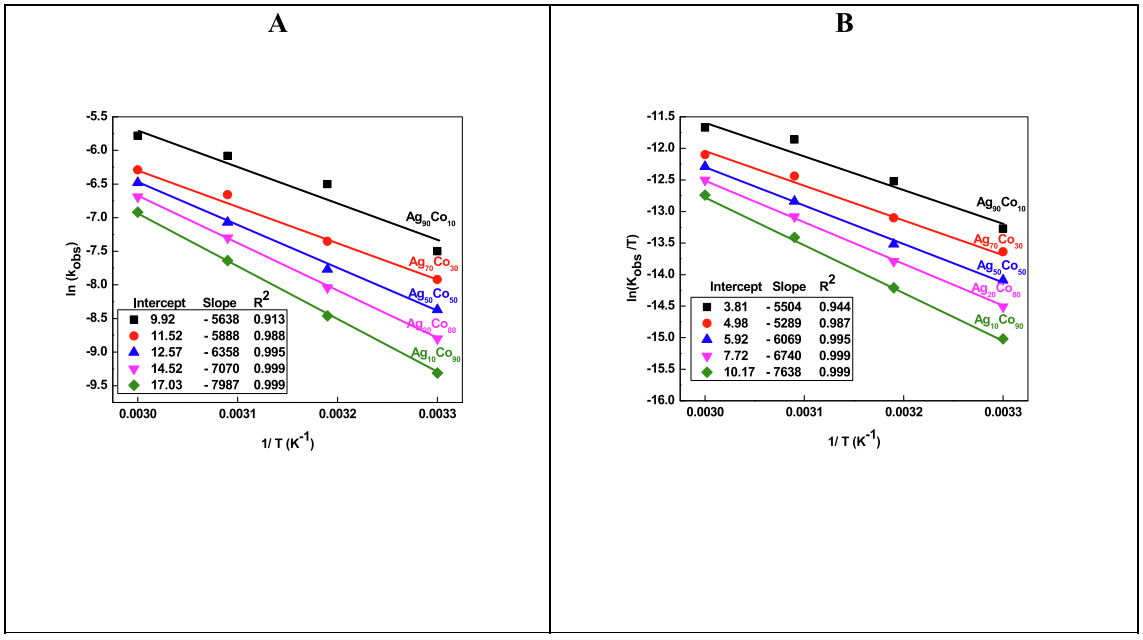

Fig. 6 Arrhenius (A) and Eyring plots (B) for the dehydrogenation of formic acid with different molar ratio of the catalyst. *Reaction conditions*: [formic acid] = 0.7 mol/L, and pH = 4.3.

Table 4 Effects of molar ratio of Ag-Co on the decomposition of formic acid ($HCOOH \rightarrow CO_2 + H_2$) at different temperature with [formic acid] = 0.7 mol/L, [Ag-Co] = 0.02 g/L, and pH = 4.3.

Ag_xCo_{100-x}	Temperature (K)	$10^4 k_{obs}$ (s^{-1})	E_a (kJ/mol)	$\Delta H^{\#}$ (kJ/mol)	$\Delta S^{\#}$ (J/K/mol)
$Ag_{10}Co_{90}$	303	5.2	46	43	−165
	313	11.4			
	323	22.7			
	333	28.2			
$Ag_{20}Co_{80}$	303	3.6	49	45	−156
	313	6.4			
	323	12.7			
	333	18.4			
$Ag_{50}Co_{50}$	303	2.3	52	50	−148
	313	4.2			
	323	8.5			
	333	15.2			
$Ag_{70}C_{30}$	303	1.5	58	56	−133
	313	3.2			
	323	6.7			
	333	12.4			
$Ag_{90}C_{10}$	303	0.9	66	63	−112
	313	2.1			
	323	4.8			
	333	9.7			

2014). For the synthesis of bimetallic NPs by using coreduction method, the metal species with the higher reduction potential is reduced first and forms a core, whereas the other metal with lower reduction potential is deposited onto the core as a shell. On the other hand, the structure of bimetallic NPs can be inversed in presence of complex forming reducing agent, stabilizing agent as well as ligand (Goia and Matijevic, 1998). In the present study, SDS (anionic surfactant) formed complex with Ag^+ and Co^{2+}, which in turn decreases the reduction potential of both metal ions to some extent (standard reduction potential values of Ag^+/Ag^0 and Co^{2+}/Co are 0.799 V and −0.28 V, respectively). As a result, the reduction of Ag^+ and Co^{2+} ions occurred simultaneously, and Ag-Co bimetallic heterostructure NPs are formed (Liu, et al., 2014).

3.5. Mechanism of formic acid dehydrogenation

Formic acid is a weak organic acid and soluble in water. On the other hand, ring-type dimeric structure of formic acid exists both in the solution and in vapor phase at room temper-

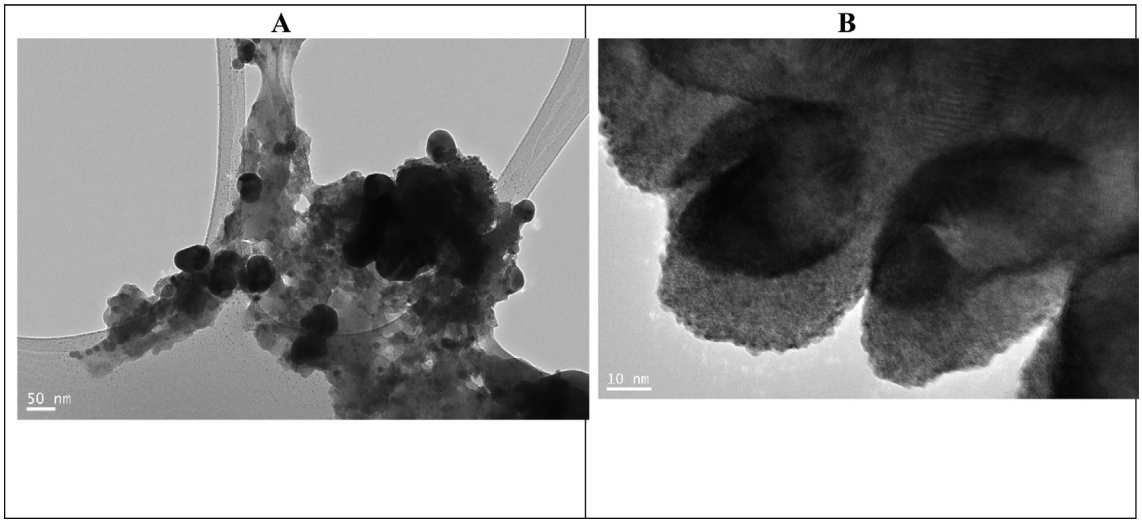

Fig. 7 TEM images of SDS free (A) and SDS capped $Ag_{10}Co_{90}$ NPs (B). *Reaction conditions*: molar ratio of Ag^+:Co^{2+} = $Ag_{10}Co_{90}$, [$NaBH_4$] = 1.0 mM, and [SDS] = 8.0 mM.

ature and normal pressure. Table 2 shows that the pH has significant effect on the dehydrogenation of formic acid. The decomposition rate was found to decrease with increasing pH of the reaction mixture. No generation of hydrogen and CO_2 was observed with higher formic acid concentration at 30 °C for ca. 1 h in absence of $A_{50}Co_{50}$. The following equilibrium must be considered to explain the effect of pH on the dehydration of formic acid (Eq. (13)).

$$HCOOH + H_2O \Longleftrightarrow HCOO^- + H_3O^+ \qquad (pK_a = 3.74) \tag{13}$$

For which we can write the Eq. (14).

$$pH = pK_a + \log\left(\frac{[HCOO^-][H_3O^+]}{[HCOOH}\right) \tag{14}$$

In an acidic solution (pH $\leq$ 4.0), formic acid mainly exists as undissociated form (HCOOH). As the pH of the solution increases, the concentration of ionized formic increases, which in turn, decreases the rate of dehydrogenation. Based on the above results and observations, Scheme 4 mechanism is proposed to the decomposition of formic acid.

In Scheme 4, HCOOH adsorbed on the surface of Ag-Co via Van der Waals interactions, and Ag-Co-HCOOH complex was formed (Eq. (15)). In the next step, decomposition of formic acid takes place due to the cleavage of O-H bond (rate determining step), which generates hydrogen and CO_2 as the final products (Eq. (16)). The rate-law (Eq.(17)) was derived for the decomposition of formic from the Scheme 4.

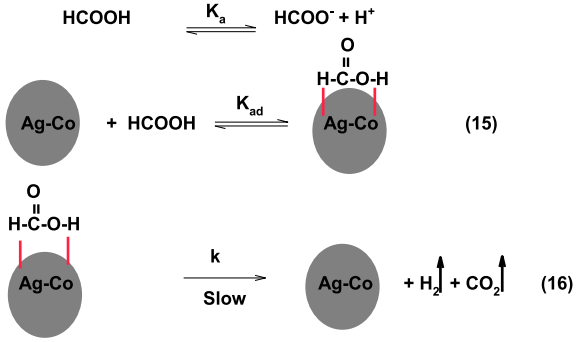

Scheme 4 Mechanism to the generation of hydrogen from formic acid in presence of $Ag_{50}Co_{50}$.

$$-\frac{d[HCOOH]}{dt} = \frac{kK_{ad}[H^+][Ag-Co][HCOOH]_T}{([H^+]+K_a)} \tag{17}$$

and, for apparent first-order rate constant, Eq. (17) can be written as Eq. (18).

$$-\frac{d[HCOOH]}{dt} = \frac{kK_{ad}[H^+][HCOOH]_T}{([H^+]+K_a)} \tag{18}$$

Eq. (18) explains the first-order dependence with respect to [formic acid] at constant [H^+]. As the [H^+] increases and decreases, the percentage of [HCOOH] decreases in the reaction mixture, which in turn, decreases the decomposition rate of formic acid at a fixed temperature. The escaping tendency of CO_2 is higher in the $HCOO^-$ than that of HCOOH but the production of hydrogen would be low at pH $\geq$ 4.0.

The number of M-hydrogen bonds (M-H) and suitable interactions were responsible to the higher catalytic activity of any catalyst for the generation of hydrogen from hydrogen storage materials (Singh and Xu, 2013; Grunze, 1979; Cheng et al., 2019) [31, 48, 49]. The catalytic performance of Ag-Co increases with increasing the cobalt content from 10 to 90%. The Ag^0 and Co^0 have zero and three un-paired electrons in the d band orbital, respectively. The adsorption of formic acid increases on the surface of the catalyst ($Ag_{10}Co_{90}$) due to the formation of higher number of M-H bonds (Nordlander et al., 1984). Formation of M-O bonds on the surface of catalyst cannot be ruled out completely.

3.6. Reusability of the catalyst

Catalyst provides a new reaction path, lower the activation energy and remain unchanged at the end of reaction. It does not take part in a chemical reaction. In order to determine the stability of $Ag_{50}Co_{50}$, the experiments were repeated with the same catalyst for six consecutive times (Fig. 8A). The catalyst exhibited no significant decrease in the activity, generat-

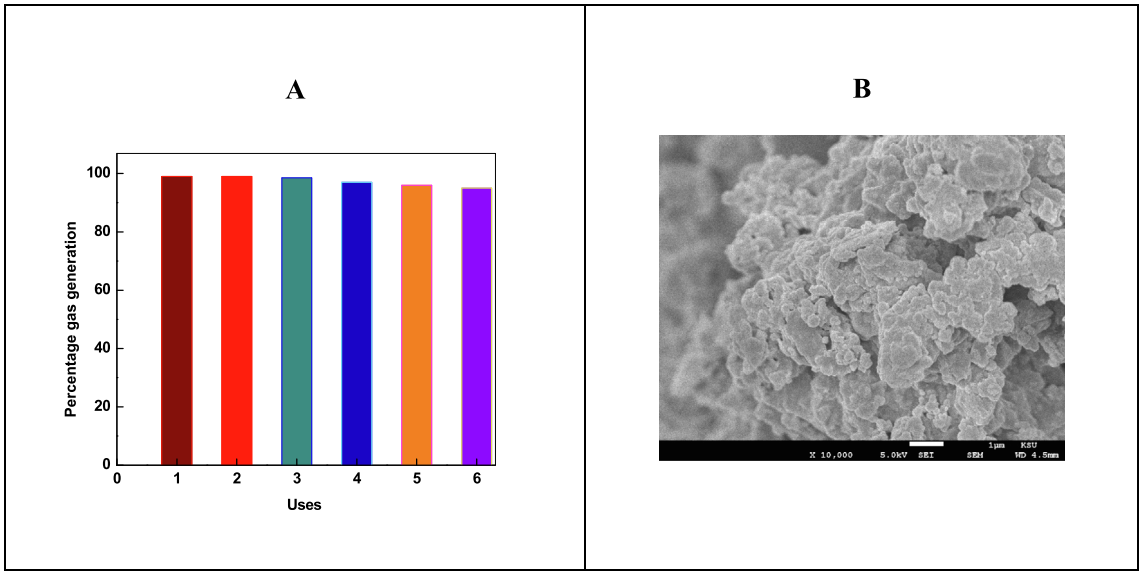

Fig. 8 Reusability of $Ag_{50}Co_{50}$ after six consecutive reactions (A), and SEM image of $Ag_{50}Co_{50}$ after the six kinetic experiment to the generation of hydrogen at 303 K. *Reaction conditions*: [formic acid] = 0.7 mol/L, [$Ag_{50}Co_{50}$] = 0.02 g/L, pH = 4.3, reaction time 2 h for A.

ing 100% hydrogen selectivity for consecutive six kinetic runs, indicating the good stability of the present bi-metallic Ag_{50}-Co_{50} NPs for decomposition of formic acid at mild reaction temperature and pH = 4.3. SEM image of the catalyst was also recorded after the decomposition of formic acid in six kinetic runs. No significant changes were observed on the surface morphology of the Ag-Co (Fig. 8B), which can be attributed to the excellent stability of the as-prepared nanocatalyst. The accurate molar ratio of Ag:Co is determined to be ca. 50:50 by the inductively coupled plasma atomic emission spectroscopy (ICP-AES) at the end of six consecutive cycles, which provides supporting evidence regarding the stability of as prepared Ag-Co to the generation of hydrogen from formic acid decomposition.

In order to compare the catalytic activity of SDS-Ag-Co nanocatalysts for the decomposition of formic acid with other catalyst, the values of activation energy are summarized in Table 5. $Pd_{0.6}Co_{0.2}Ni_{0.2}$/N-CN (Dong, et al., 2019) and AgPd/2D g-C_3N_4 (Wan, et al., 2020) required low activation energy for the decomposition of formic acid. Inspection of Table 5 clearly indicates that the catalytic activity of the catalyst strongly depends on the incorporation of second and third metal into the monometallic NPs, ratio of all metal salt precursor, nature of all metals, and presence of stabilizing agent (surfactant, graphene, polymer, and others). SDS-$Ag_{90}Co_{10}$ exhibits higher catalytic activity than that of Au/Al_2O_3 and Pt/Al_2O_3 (Table 5).

Table 5 Values of activation energy for the dehydrogenation of formic acid ($HCOOH \rightarrow CO_2 + H_2$) by various catalysts.

Catalyst	Activation energy (kJ/mol)	Reference
$Pd_{0.6}Co_{0.2}Ni_{0.2}$/N-CN	20	Dong et al., 2019
AgPd/2D g-C_3N_4	24	Wan et al., 2020
Pd/Ag/Fe	66	Khan, 2019
Fe/Pd/Ag	60	Khan, 2019
Fe/Ag/Pd	51	Khan, 2019
$Co_6Ag_{0.1}Pd_{0.9}$/RGO	43	Chen et al., 2015
Au/Al_2O_3	53	Ojeda and Iglesia, 2009
Pt/Al_2O_3	52	Ojeda and Iglesia, 2009
Pd/MSC-30	38	Chen et al., 2015
Pd/EDA-HPAN	39	Li et al., 2022
$PdCo_{0.2}$/EDA-HPAN	37	Li et al., 2022
$Ag_{10}Co_{90}$	46	Present work
$Ag_{20}Co_{80}$	49	Present work
$Ag_{50}Co_{50}$	52	Present work
$Ag_{70}C_{30}$	58	Present work
$Ag_{90}C_{10}$	66	Present work

4. Conclusion

In this work, SDS free and SDS-Ag-Co NPs were prepared by using step-wise chemical reduction method. Formic acid decomposition was investigated under mild experimental conditions by using SDS free and SDS-Ag-Co nanocatalysts. The presence of SDS significantly increases the hydrogen generation from the formic acid by Ag-Co. The activation energy deceases from 66 to 44 kJ/mol with increasing the Co content. The major cause for the higher catalytic performance was attributed to the Co percentage in the Ag-Co. The use of SDS as a strong complexing agent is the main key point of the present studies. The higher Co ratio and the presence of SDS as support would enhanced the practical application of formic acid to the production of hydrogen for the fuel cell.

Declaration of Competing Interest

The authors declare that they have no known competing financial interests or personal relationships that could have appeared to influence the work reported in this paper.

Acknowledgement

This project was funded by the Deanship of Scientific Research (DSR) at King Abdulaziz University, Jeddah, under grant no. (G-109-247-1441). The authors, therefore, acknowledges with thanks DSR for technical and financial support.

References

Akbayrak, S., Tonbul, Y., Ozkar, S., 2017. Nanoceria supported palladium(0) nanoparticles: Superb catalyst in dehydrogenation of formic acid at room temperature. Appl. Catal. B Environ. 206, 384–392.

Albeladi, A.B., Al-Thabaiti, S.A., Khan, Z., 2020. Effect of CTAB on the surface resonance plasmon intensity of silver nanoparticles: Stability and oxidative dissolution. J. Mol. Liq. 302, 112565.

Alsubaie, H., Zaheer, Z., Aazam, E.S., 2021. Role of ionic surfactants on the nucleation and growth of silver nanoparticles. J. Mol. Liq. 341, 117309.

Al-Thabaiti, S.A., Khan, Z., Malik, M.A., 2019. Bimetallic Ag-Ni nanoparticles as an effective catalyst for hydrogen generation from hydrolysis of sodium borohydride. Int. J. Hydrogen Energy 44, 16452–16466.

Al-Thubaiti, K.S., Khan, Z., 2020. Trimetallic nanocatalysts to enhanced hydrogen production from hydrous hydrazine: The role of metal centers. Int. J. Hydrogen Energy 45, 13960–13974.

Ben Aziza, W., Petit, J.F., Demirci, U.B., Xu, Q., Miele, P., 2014. Bimetallic nickel-based nanocatalysts for hydrogen generation from aqueous hydrazine borane: investigation of iron, cobalt and palladium as the second metal. Int. J. Hydrogen Energy 39, 16919-16926.

Bunton, C.A., 2006. The dependence of micellar rate effects upon reaction mechanism. Adv. Colloid Interf. Sci. 123–126, 333–343.

Cao, N., Tan, S.Y., Luo, W., Hu, K., Cheng, G.Z., 2016. Ternary CoAgPd nanoparticles confined inside the pores of MIL-101 as efficient catalyst for dehydrogenation of formic acid. Catal. Lett. 146, 518–524.

Chen, Y., Zhu, Q.-L., Tsumori, N., Xu, Q., 2015. Immobilizing highly catalytically active noble metal nanoparticles on reduced graphene oxide: a non-noble metal sacrificial approach. J. Am. Chem. Soc. 137, 106–109.

Cheng, Y., Wu, X., Xu, H., 2019. Catalytic decomposition of hydrous hydrazine for hydrogen production. Sustainable Energy Fuels 3, 343–365.

Coffey, R.S., 1967. The decomposition of formic acid catalysed by soluble metal complexes. Chem. Commun., 923–924

Dong, Z., Li, F., He, Q., Xiao, X., Chen, M., Wang, C., Fan, X., Chen, L., 2019. PdCoNi nanoparticles supported on nitrogen-doped porous carbon nanosheets for room temperature dehydrogenation of formic acid. Int. J. Hydrogen Energy 44, 11675–11683.

Ferrando, R., Jellinek, J., Johnston, R.L., 2008. Nanoalloys: from theory to applications of alloy clusters and nanoparticles. Chem. Rev. 108, 845–910.

Goia, D.V., Matijevic, E., 1998. Preparation of monodispersed metal particles. New J.Chem. 22, 1203–1215.

Grad, O., Mihet, M., Dan, M., Blanita, G., Berghian-Grosan, C., Lazar, M.D., 2019. Au/reduced graphene oxide composites: Eco-friendly preparation method and catalytic applications for formic acid dehydrogenation. J. Mater. Sci. 54, 6991–7004.

Grunze, M., 1979. The interaction of hydrazine with an surface Fe (111). Surf. Sci. 81, 603–625.

Guo, Z., Chen, Y., Li, L., Wang, X., Haller, G.L., Yang, Y., 2010. Carbon nanotube supportedPt-based bimetallic catalysts prepared by a microwave-assisted polyol reduction method and their catalytic applications in the selective hydrogenation. J. Catal. 276, 314–326.

Gurtu, A., Bakshi, M.S., 2018. Ag nanometallic surfaces for self-assembled ordered morphologies of zein. ACS Omega 3, 10851–10857.

Hu, C., Ting, S.-W., Tsui, J., Chan, K.-Y., 2012. Formic acid dehydrogenation over PtRuBiOx/C catalyst for generation of CO-free hydrogen in a continuous-flow reactor. Int. J. Hydrogen Energy 37, 6372–6380.

Huber, G.W., Iborra, S., Corma, A., 2006. Synthesis of transportation fuels from biomass: Chemistry, catalysts, and engineering. Chem. Rev. 106, 4044–4098.

Irankhah, A., Fattahi, S.M.S., Salem, M., 2018. Hydrogen generation using activated aluminum/water reaction. Int. J. Hydrogen Energy. 43, 15739–15748.

Jeon, H.-J., Chung, Y.-M., 2017. Hydrogen production from formic acid dehydrogenation over Pd/C catalysts: Effect of metal and support properties on the catalytic performance. Appl. Catal. B Environ. 210, 212–222.

Johnson, T.C., Morris, D.J., Wills, M., 2010. Hydrogen generation from formic acid and alcohols using homogeneous catalysts. Chem. Soc. Rev. 39, 81–88.

Karahan, S., Ozkar, S., 2015. Poly(4-styrenesulfonic acid-co-maleic acid) stabilized cobalt(0) nanoparticles: a cost-effective and magnetically recoverable catalyst in hydrogen generation from the hydrolysis of hydrazine borane. Int. J. Hydrogen Energy 40, 2255-2265.

Khan, Z., 2020. Chitosan capped Au@Pd@Ag trimetallic nanoparticles: Synthesis, stability, capping action and adsorbing activities Int. J. Biol. Macromol. 153, 545–560.

Khan, Z., 2019. Trimetallic nanoparticles: Synthesis, characterization and catalytic degradation of formic acid for hydrogen generation. Int. J. Hydrogen Energy 44, 11503–11513.

Khan, Z., Al-Thabaiti, S. A., Obaid, A.Y., Malik, M.A., Khan, M.N., Khan, T.A., 2016. Cobalt@silver bimetallic nanoparticles: Solution based seedless surfactant assisted synthesis, optical properties, and morphology. J. Mol. Liq. 222, 272-278.

Kosa, S.A., Zaheer, Z., 2019. Betanin assisted synthesis of betanin@silver nanoparticles and their enhanced adsorption and biological activities. Food Chem. 298, 125014.

Li, Y., She, P., Ding, R., Li, D., Cai, H., Hao, X., Jia, M., 2022. Bimetallic PdCo nanoparticles loaded in amine modified polyacrylonitrile hollow spheres as efficient catalysts for formic acid dehydrogenation. Catalysts 12, 33.

Liu, H., Li, X.-X., Liu, X.-Y., Ma, Z.-H., Yin, Z.-Y., Yang, W.-W., Yu, Y.-S., 2021. Schiff-base-rich g-CxN_4 supported PdAg nanowires as an efficient Mott-Schottky catalyst boosting photocatalytic dehydrogenation of formic acid. Rare Met. 40, 808–816.

Liu, W.-J., Qian, T.-T., Jiang, H., 2014. Bimetallic Fe nanoparticles: Recent advances in synthesis and application in catalytic elimination of environmental pollutants. Chem. Eng. J. 236, 448–463.

Luo, Y.-C., Liu, Y.-H., Hung, Y., Liu, X.-Y., Mou, C.-Y., 2013. Mesoporous silica supported cobalt catalysts for hydrogen generation in hydrolysis of ammonia borane. Int. J. Hydrogen Energy 38, 7280–7290.

Mihet, M., Dan, M., Barbu-Tudoran, Lazar, L.M.D., Blanita, G., 2020. Controllable H_2 generation by formic acid decomposition on a novel Pd/template carbon catalyst. Hydrogen 1, 22–37.

Moulder, J. F., Chastain, J., 1992. Handbook of x-ray photoelectron spectroscopy. A reference book of standard spectra for identification and interpretation of XPS data. Eden Prairie, Minnesota: Physical Electronics Division, Perkin-Elmer Corp.

Muir, S.S., Yao, X., 2011. Progress in sodium borohydride as a hydrogen storage material: Development of hydrolysis catalysts and reaction systems. Int. J. Hydrogen Energy 36, 5983–5997.

Navarro, R.M., Pena, M.A., Fierro, J.L.G., 2007. Hydrogen production reactions from carbon feed stocks: Fossil fuels and biomass. Chem. Rev. 107, 3952–3991.

Nordlander, P., Holloway, S., Norskov, J.K., 1984. Hydrogen adsorption on metal surfaces. Surf. Sci. 136, 59–81.

Ojeda, M., Iglesia, E., 2009. Formic acid dehydrogenation on Au-based catalysts at near- ambient temperatures Angew. Chem. Int. Ed. 48, 4800–4803.

Ortiz-Quinonez, J.-L., Pal, U., 2019. Borohydride-assisted surface activation of $Co_3O_4/CoFe_2O_4$ composite and its catalytic activity for 4-Nitrophenol reduction. ACS Omega 4, 10129–10139.

Sen, B., Kuzu, S., Demir, E., Akocak, S., Sen, F., 2017. Highly monodisperse RuCo nanoparticles decorated on functionalized multiwalled carbon nanotube with the highest observed catalytic activity in the dehydrogenation of dimethylamine_borane. Int. J. Hydrogen Energy 42, 23292–23298.

Shen, K., Chen, L., Long, J.L., Zhong, W., Li, Y.W., 2015. MOFs-templated Co@Pd core shell NPs embedded in N-doped carbon matrix with superior hydrogenation activities. ACS Catal. 5, 5264–5271.

Singh, S.K., Xu, Q., 2009. Complete conversion of hydrous hydrazine to hydrogen at room temperature for chemical hydrogen storage. J. Am. Chem. Soc. 131, 18032–18033.

Singh, S.K., Xu, Q., 2010. Bimetallic nickel-iridium nanocatalysts for hydrogen generation by decomposition of hydrous hydrazine. Chem. Commun. 46, 6545–6547.

Singh, S.K., Xu, Q., 2013. Nanocatalysts for hydrogen generation from hydrazine. Catal. Sci. Technol. 3, 1889–1900.

Tedsree, K., Li, T., Jones, S., Chan, C.W.A., Yu, K.M.K., Bagot, P.A. J., Marquis, E.A., Smith, G.D.W., Tsang, S.C.E., 2011. Hydrogen production from formic acid decomposition at room temperature using a Ag–Pd core–shell nanocatalyst. Nature Nanotechnology 6, 302–307.

Wan, C., Zhou, L., Xu, S., Jin, B., Ge, X., Qian, X., Xu, L., Chen, F., Zhan, X., Yang, Y., Cheng, D.-G., 2022. Defect engineered mesoporous graphitic carbon nitride modified with AgPd nanoparticles for enhanced photocatalytic hydrogen evolution from formic acid. Chem. Eng. J. 429, 132388.

Wan, C., Zhou, L., Sun, L., Xu, L., Cheng, D.-G., Chen, F., Zhan, X., Yang, Y., 2020. Boosting visible-light-driven hydrogen evolution from formic acid over AgPd/2D g-C_3N_4 nanosheets Mott-Schottky photocatalyst. Chem. Eng. J. 396, 125229.

Wang, Z.-L., Ping, Y., Yan, J.-M., Wang, H., Jiang, Q., 2014. Hydrogen generation from formic acid decomposition at room temperature using a NiAuPd alloy nanocatalyst. Int. J. Hydrogen Energy 39, 4850–4856.

Wang, Z.-L., Yan, J.-M., Ping, Y., Wang, H.-L., Zheng, W.-T., Jiang, Q., 2013. An Efficient CoAuPd/C catalyst for hydrogen generation from formic acid at room temperature. Angew. Chem. Int. Ed. 52, 4406–4409.

Yadav, M., Xu, Q., 2013. Catalytic chromium reduction using formic acid and metal nanoparticles immobilized in a metal-organic framework. Chem. Commun. 49, 3327–3329.

Yang, J., Cheng, F., Liang, J., Chen, J., 2011. Hydrogen generation by hydrolysis of ammonia borane with a nanoporous cobalt-tungsten-boron-phosphorus catalyst supported on Ni foam. Int. J. Hydrogen Energy 36, 1411–1417.

Yang, L., Hua, X., Su, J., Luo, W., Chen, S., Cheng, G., 2015. Highly efficient hydrogen generation from formic acid-sodium formate over monodisperse AgPd nanoparticles at room temperature. Appl. Catal. B Environ. 168–169, 423–428.

Yang, Y., Xu, H., Cao, D., Zeng, X.C., Cheng, D., 2019. Hydrogen production via efficient formic acid decomposition: Engineering the surface structure of Pd-based alloy catalysts by design. ACS Catal. 9, 781–790.

Yao, C.F., Zhuang, L., Cao, Y.L., Ai, X.P., Yang, H.X., 2008. Hydrogen release from hydrolysis of borazane on Pt- and Ni- based alloy catalysts. Int. J. Hydrogen Energy 33, 2462–2467.

Yasaka, Y., Yoshida, K., Wakai, C., Matubayasi, N., Nakahara, M., 2006. Kinetic and equilibrium study on formic acid decomposition in relation to the water-gas-shift reaction. J. Phys. Chem. A 110, 11082–11090.

Zacharska, M., Chuvilin, A.L., Kriventsov, V.V., Beloshapkin, S., Estrada, M., Simakov, A., Bulushev, D.A., 2016. Support Effect for nanosized Au catalysts in hydrogen production from formic acid decomposition. Catal. Sci. Technol. 6, 6853–6860.

Zaheer, Z., 2021. Chitosan capped noble metal doped CeO_2 nanomaterial: Synthesis, and their enhanced catalytic activities. Int. J. Biol. Macromol. 166, 1258–1271.

Zaheer, Z., AL-Asfar, A., Aazam, E.S., 2019. Adsorption of methyl red on biogenic Ag@Fe nanocomposite adsorbent: Isotherms, kinetics and mechanisms. J. Mol. Liq. 283, 287–298.

Zaheer, Z., Albukhari, S.M., 2020. Fabrication of zinc/silver binary nanoparticles, their enhanced microbial and adsorbing properties. Arabian J. Chem. 13, 7921-7938.